

**Direct observation of the band structure in bulk hexagonal boron nitride**

Hugo Henck,<sup>1</sup> Debora Pierucci,<sup>1</sup> Giorgia Fugallo,<sup>2,3</sup> José Avila,<sup>4</sup> Guillaume Cassabois,<sup>5</sup> Yannick J. Dappe,<sup>6</sup> Mathieu G. Silly,<sup>4</sup> Chaoyu Chen,<sup>4</sup> Bernard Gil,<sup>5</sup> Matteo Gatti,<sup>2,3,4</sup> Francesco Sottile,<sup>2,3</sup> Fausto Sirotti,<sup>4</sup> Maria C. Asensio,<sup>4</sup> and Abdelkarim Ouerghi<sup>1,\*</sup>

<sup>1</sup>Centre de Nanosciences et de Nanotechnologies, CNRS, Université Paris-Sud, Université Paris-Saclay, C2N–Marcoussis, 91460 Marcoussis, France

<sup>2</sup>Laboratoire des Solides Irradiés, École Polytechnique, CNRS, CEA, Université Paris-Saclay, F-91128 Palaiseau, France

<sup>3</sup>European Theoretical Spectroscopy Facility (ETSF)

<sup>4</sup>Synchrotron-SOLEIL, Saint-Aubin, Boîte Postale 48, F91192 Gif sur Yvette Cedex, France

<sup>5</sup>Laboratoire Charles Coulomb (L2C), UMR 5221 CNRS-Université de Montpellier, F-34095, Montpellier, France

<sup>6</sup>SPEC, CEA, CNRS, Université Paris-Saclay, CEA Saclay 91191 Gif-sur-Yvette Cedex, France

(Received 15 November 2016; revised manuscript received 18 January 2017; published 8 February 2017)

A promising route towards nanodevice applications relies on the association of graphene and transition metal dichalcogenides with hexagonal boron nitride (*h*-BN). Due to its insulating nature, *h*-BN has emerged as a natural substrate and gate dielectric for graphene-based electronic devices. However, some fundamental properties of bulk *h*-BN remain obscure. For example, the band structure and the position of the Fermi level have not been experimentally resolved. Here, we report a direct observation of parabolic dispersions of *h*-BN crystals using high-resolution angle-resolved photoemission spectroscopy (ARPES). We find that *h*-BN exfoliation on epitaxial graphene enables overcoming the technical difficulties of using ARPES with insulating materials. We show trigonal warping of the intensity maps at constant energy. The valence-band maxima are located around the *K* points, 2.5 eV below the Fermi level, thus confirming the residual *p*-type character of typical *h*-BN.

DOI: [10.1103/PhysRevB.95.085410](https://doi.org/10.1103/PhysRevB.95.085410)

**I. INTRODUCTION**

Two-dimensional materials have received increasing attention since the discovery of graphene. Hexagonal boron nitride (*h*-BN), a structural analog of graphene, possesses only a 1.7% lattice mismatch with graphene, but, in contrast, a large band gap ( $\sim 6$  eV). These *h*-BN films have a wide range of attractive properties, including high temperature stability, high mechanical strength, and high thermal conductivity leading to a large variety of potential applications.

Graphene is considered to be an ideal material for the fabrication of nanoelectronic devices due to its excellent electrical properties. Therefore, it has been suggested that because of the close matching of the lattice parameters between *h*-BN and graphene, *h*-BN on graphene would give rise to a band gap opening of graphene. It is argued that *h*-BN could serve as a good gate dielectric material for graphene transistors [1]. As a perfect dielectric layer, *h*-BN has an atomically flat and dangling-bond-free surface, which reduces impurity bonding and the formation of charged traps associated with the graphene/dielectric interface. In particular, graphene/*h*-BN vertical stacks exhibit extremely high carrier mobility [2,3]. The combinations of graphene, transition metal dichalcogenide ( $\text{MX}_2$ ), and *h*-BN, including both stacked graphene/*h*-BN and  $\text{MX}_2$ /*h*-BN structures, have also demonstrated very intriguing physical properties [4–8]. The availability of high-quality *h*-BN flakes also paves the way to the application of *h*-BN in far-ultraviolet light-emitting diodes and transparent electronics, due to its excellent mechanical strength [9], chemical inertness, [2] and optical transparency. These attractive properties of *h*-BN have led, in the last few years, to finding ways of synthesizing it and targeting

its large domain size, uniform thickness, and then creating high-quality multilayer *h*-BN in order to offer the best context for studying its electronic properties [10–13]. However, due to its insulating nature, the band structure of *h*-BN has not been studied experimentally in its bulk form [14–16], but only in monolayers. To our knowledge, few studies have looked at the band structure of *h*-BN at the single-layer level, where the electronic interaction between single-layer *h*-BN and the substrate cannot easily be estimated. Usachov *et al.* [15] used Au intercalation in order to decouple a *h*-BN layer from a Ni substrate. They obtained a quasifreestanding *h*-BN single layer and confirmed this by observing its band structure through angle-resolved photoemission spectroscopy (ARPES). In contrast to multilayer graphene or graphite, the usual spectroscopic characterization techniques such as x-ray photoemission spectroscopy (XPS) and ARPES are not easy to use with bulk *h*-BN [17] due to its insulating nature, as well as in some cases, its micrometric sample size.

Here, we demonstrate for the feasibility of angle-resolved spectroscopy (XPS/ARPES) with a *h*-BN crystal. Instead of using *h*-BN as a substrate for graphene, we adopted the opposite strategy by using graphene as an ideal substrate for studying the electronic band structure of *h*-BN. We found that depositing *h*-BN on graphene overcame the technical difficulty of carrying out ARPES on insulating *h*-BN. The high quality of the *h*-BN material transferred onto the graphene underlayer was proved by atomic force microscopy (AFM) and Raman spectroscopy measurements. Consequently, a detailed study of the structural properties and electronic band structure of exfoliated *h*-BN was carried out using XPS and nano-ARPES measurements, together with band-structure calculations. We have calculated an effective mass of about  $-0.49m_e$  which is roughly equal to the measured experimental value. We provide a comprehensive explanation of the *h*-BN electronic structure,

\*[abdelkarim.ouerghi@c2n.upsaclay.fr](mailto:abdelkarim.ouerghi@c2n.upsaclay.fr)

fundamentally important for a better understanding and control of the band offset between bulk *h*-BN and two-dimensional (2D) materials.

## II. METHODS

Mechanical deposition of *h*-BN flakes on a graphene layer was carried out using the standard Scotch tape technique. Our crystal is a commercial *h*-BN crystal from HQ Graphene. AFM measurements were performed on a Veeco AFM with a scan rate of 0.299 Hz and a resolution of 512 points per line. Raman measurements were carried out using a commercial confocal Renishaw micro-Raman microscope with a 100 $\times$  objective, a Si detector (detection range up to  $\sim$ 2.2 eV), and a 532-nm laser at room temperature. To ensure the reproducibility of the data, we followed a careful alignment and optimization protocol. In addition, the excitation laser was focused onto the samples with a spot diameter of  $\sim$ 1  $\mu$ m and incident power of  $\sim$ 5 mW. The integration time was optimized to obtain a satisfactory signal-to-noise ratio. XPS experiments were carried out on the TEMPO beamline [18] (SOLEIL French synchrotron facility) at room temperature. A Shirley background was subtracted in all core level spectra. The B 1s and N 1s spectra were fitted using sums of Voigt curves, that is, the convolution of a Gaussian by a Lorentzian, in which the full width at half maximum was fixed at 70 meV for the B 1s [19] and 115 meV for the N 1s [20], respectively. For the used photon energy of 820 eV we had a full width at half maximum (FWHM)  $\sim$ 1 eV (overall resolution of  $\sim$ 150 meV). The spot size was 100  $\times$  80  $\mu$ m<sup>2</sup>. Nano ARPES experiments were performed on the ANTARES beamline (SOLEIL French synchrotron facility). The ARPES data were taken at a photon energy of 100 eV, using linearly polarized light, a base pressure of 5  $\times$  10<sup>-11</sup> mbar, and keeping the sample cooled at ca. 40 K. More details on the material configuration are given in the Supplemental Material, S1 [21]. Band-structure calculations, performed with the ABINIT code [22], are in good agreement with results from the literature [23–26]. Computational details are summarized in the Supplemental Material, S4 [21].

## III. RESULTS AND DISCUSSIONS

Among different graphene substrates, the use of epitaxial graphene on silicon carbide provides several potential advantages for the electronic study of *h*-BN, as well as its interaction with graphene [27–32]. In particular, these include high electron mobility [33,34], tunable substrate coupling [35], wafer-scale processability, and crystalline ordering that can provide templates commensurate with the substrate. The graphene used in this work was obtained by annealing 4H-SiC(0001) at 1550  $^{\circ}$ C in 800 mbar argon for 10 min [36,37]. Figure 1(a) presents the crystal structure of the layered *h*-BN. Each single layer of *h*-BN consisted of B and N atoms arranged in the two inequivalent A and B sublattices of the hexagonal lattice structure. For this structure, AA' stacking with each B atom on top of a N atom is mostly observed [38,39]. The BN and BB bond lengths are about 1.45 and 2.52  $\text{Å}$ , respectively [40]. The interlayer separation of the bulk is 3.33  $\text{Å}$  [17,40,41]. The graphene underlayer presented a very inert surface ensuring the presence of only van der

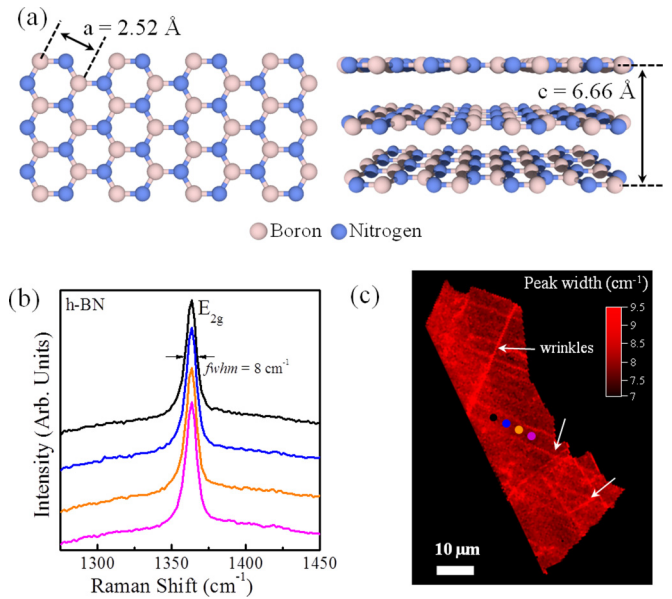


FIG. 1. Crystal structure and micro-Raman spectroscopy of multilayer *h*-BN: (a) crystal structure of *h*-BN, (b) and (c) micro-Raman spectra and map taken on the *h*-BN/graphene layer. The Raman spectra of (b) have been measured along a terrace of the SiC substrate at the location indicated by the corresponding colored dots in (c).

Waals (vdW) interactions between *h*-BN and graphene. The mild roughness of the graphene surface guaranteed a reduced strain on multilayer *h*-BN and a negligible impact on the band structure and the Fermi energy level.

Micro-Raman spectroscopy was used to characterize the quality and crystalline form of a large multilayer *h*-BN sample (20  $\times$  100  $\mu$ m<sup>2</sup>). Several spectra representing the fundamental stretching mode in different sample positions are shown in Fig. 1(b). The  $E_{2g}$  mode was centered at  $\sim$ 1365  $\text{cm}^{-1}$ , the expected value for bulk *h*-BN [4], suggesting that no stress was induced by the graphene substrate. The linewidth of this peak, estimated from a Lorentzian fitting, was very small at only  $8 \pm 0.5 \text{ cm}^{-1}$ . This intense and narrow Raman peak indicated the high-crystalline structure of the *h*-BN flake with minimal defects [42]. Figure 1(c) shows the map of the  $E_{2g}$  mode full width at half maximum (FWHM). The FWHM on the terraces was 8  $\text{cm}^{-1}$  (with a variation below 0.5  $\text{cm}^{-1}$ ) indicating the homogeneity of *h*-BN on the whole flake. An increase in FWHM was observed at surface steps and in particular on the few wrinkles, highlighted by white arrows in Fig. 1(c), where a FWHM of about  $9.5 \pm 0.5 \text{ cm}^{-1}$  was obtained. Moreover, only this  $E_{2g}$  mode was observed. This is characteristic of the hexagonal BN structure, cubic BN giving rise to Raman modes at 1056  $\text{cm}^{-1}$  (TO phonon) and 1306  $\text{cm}^{-1}$  (LO phonon). Such Raman spectra have only been reported for the highest-quality *h*-BN grown using the liquid-metal method [11]. Our measurements thus showed that the quality of our *h*-BN film was similar to that of single-crystal *h*-BN. A typical AFM image of the sample is reported in Fig. 2(a). The underlying graphene on SiC presented large terraces ( $\sim$ 6  $\mu$ m), separated by straight step edges. The *h*-BN flake was clearly completely flat, following perfectly the morphology of the graphene/SiC underlayer. The

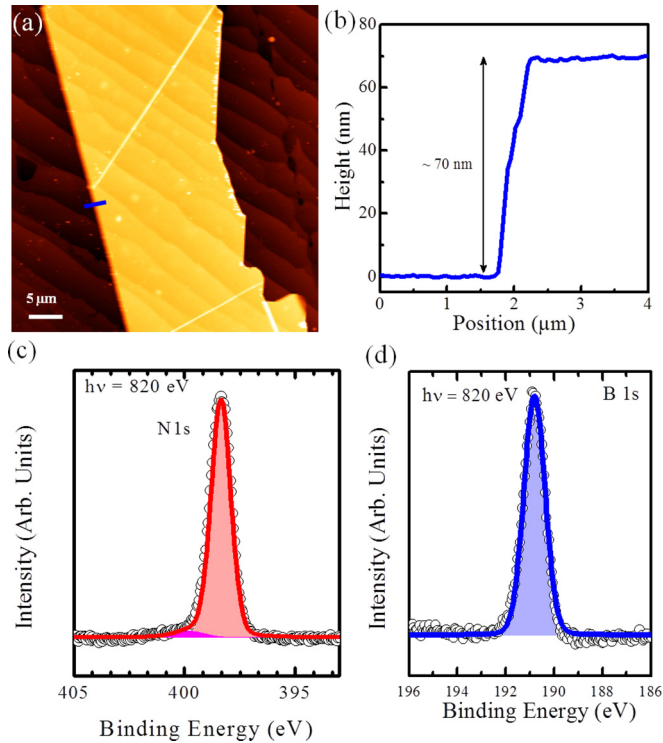


FIG. 2. AFM images and XPS spectra of *h*-BN: (a) AFM image of *h*-BN/graphene, (b) AFM height profile corresponding to the blue line in (a). (c), (d) are high-resolution XPS spectra at  $h\nu = 820$  eV of N 1s and B 1s core levels, respectively.

average size of the *h*-BN terraces was limited by the SiC terrace dimensions. One important observation is that the *h*-BN layer was clearly continuous over the step edge without dislocations or fractures, indicating the possibility of large-scale transfer of *h*-BN. This structural coherency across steps was also shown in the micro-Raman images. The profile scan presented in Fig. 2(b) allowed us to measure the height of the flake and we obtained an estimation of the number of layers to be about 210 ( $c/2 = 3.3$  Å). The high number of layers ensured the bulk nature of the *h*-BN flake.

The chemical bonding environment of the *h*-BN flake was investigated using high-resolution XPS. We used 820 eV photon energy. The boron 1s (B 1s) and nitrogen 1s (N 1s) spectra are shown in Figs. 2(c) and 2(d), respectively. The experimental data are displayed as dots, while the solid line is the sum of the fitted components. One main sharp peak (FWHM = 1.0 eV) was recorded in both spectra, measured at binding energies (BEs) 190.8 and 398.4 eV, for B and N, respectively. This suggests a main chemical environment corresponding to the B-N bond in the hexagonal structure [4,43–47], as expected for a *h*-BN crystal. In the B 1s spectrum no shoulders are present at lower binding energies, indicative of B-C [48,49] or N-C [48,49] binding, or at higher binding energies, expected for B-O [17,50], N-N [17,49], or N-O [17,49,51]. A very small shoulder is present in the N 1s spectrum at higher BE (about 1.4 eV). This peak is the signature of interstitial nitrogen defects which is bound with N atoms of the lattice forming a N-N pair [52]. This type of defect is expected in particular for a *p*-type *h*-BN. The

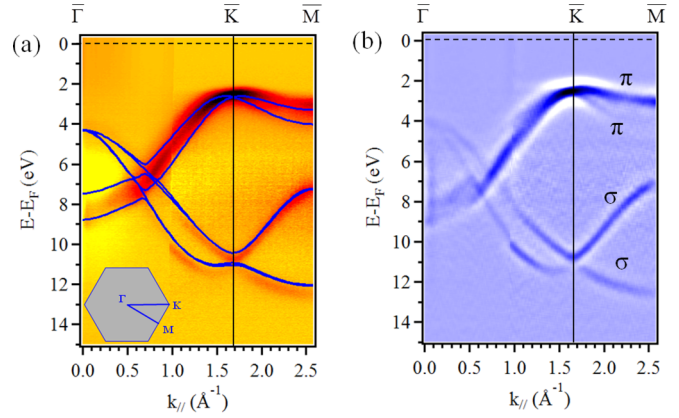


FIG. 3. Electronic structure of bulk *h*-BN: (a) nano-ARPES spectra of *h*-BN at  $h\nu = 100$  eV and calculated GW band structure (blue lines) of bulk *h*-BN for  $k_z = 0.3\pi/c$ . The inset of (a) shows the Brillouin zone of graphene and *h*-BN with a twist angle of  $30^\circ$ . (b) Second-derivative spectra of (a) to enhance the visibility of the bands. Black dashed lines indicate the Fermi level position.

very low defect concentration confirms the high quality of the *h*-BN crystal obtained after the transfer process on epitaxial graphene.

Although Raman, AFM, and XPS are standard characterization techniques, which can be routinely used with *h*-BN samples, ARPES measurements for *h*-BN have not been reported so far due to the large band gap of this material, which induces a charging effect detrimental to ARPES. Here we demonstrate a strategy that can circumvent this issue and provide experimental determination of the *h*-BN band structure. Thanks to the graphene underlayer, the absence of an electrostatic charging effect of the transferred *h*-BN flakes, as well as its high structural and electronic quality, have made it possible to study the electronic structure in the low-energy range. Moreover, nano-ARPES enabled us to focus the x-ray beam on a spot size of  $\sim 120$  nm on the *h*-BN flakes in order to reach detailed band-structure measurements [53,54]. Due to the transfer process, the graphene and *h*-BN flake is arbitrarily rotated through a certain twist angle. Using ARPES constant energy maps recorded outside [Fig. S2(a)], and inside the *h*-BN flake [Fig. S2(b)], we found that the *h*-BN Brillouin zone (BZ) was rotated by  $30^\circ$  with respect to the graphene BZ [inset of Fig. S3(c)] from the constant energy map of the graphene layer and *h*-BN, where a sixfold-symmetry structure is observed.

In Fig. 3(a), the photoelectron intensity (for a photon energy  $h\nu = 100$  eV) in *h*-BN is shown as a function of binding energy and the wave vector  $k_{\parallel}$  along a path in a plane parallel to  $\Gamma KM$  [in the following we will adopt the hexagonal surface BZ name convention for high-symmetry  $k$  points; see inset in Fig. 3(a)]. The second-derivative spectrum is provided in Fig. 3(b) to improve the band-structure visibility. The  $\pi$  states of *h*-BN are degenerate at the  $\bar{K}$  point of the hexagonal BZ. In the intensity map, two parabolic bands disperse in the  $\bar{\Gamma}\bar{K}$  and  $\bar{M}\bar{K}$  directions towards the valence-band maximum, as clearly shown in the derivative spectrum. The *h*-BN  $\pi$  bands are the prominent features that disperse from a binding energy of 9 eV at the  $\bar{\Gamma}$  point, up to about 2.5 eV near the  $\bar{K}$  point, and down to about 2.8 eV at the  $\bar{M}$  point. These bands are degenerate at  $\bar{K}$

[a closeup of Fig. 3 is shown in Fig. S3(a)], with a maximum splitting of 1–2 eV at  $\bar{\Gamma}$  [Fig. 3(b)]. The presence of this  $\pi$ -band splitting, clear signature of a bulk  $h$ -BN band structure, is confirmed also by the two bands observed around the  $\bar{M}$  point along the  $\bar{\Gamma}\bar{M}$  direction of the  $h$ -BN first BZ [Fig. S3(b)]. This splitting arises from the coupling between BN layers. Indeed, by increasing the interlayer distance, the splitting is reduced [41], while in the limiting case of a monolayer there is just a single  $\pi$  band [22,55].

The BN  $\sigma$  bands are well resolved, dispersing downwards from 4 eV at the  $\bar{\Gamma}$  point, where they are degenerate, to 12 eV at the  $\bar{K}$  point. The high intensity and good resolution of the  $\pi$  and  $\sigma$  bands attest to the high quality of the  $h$ -BN sample. Moreover, the signatures of rotated domains of  $h$ -BN are not observed [Figs. S2(b)]. This finding suggests the presence of only a single orientation of the  $h$ -BN and the absence of rotational disorder and twinning domains.

The ARPES spectra were compared with state-of-the-art band-structure calculations for bulk  $h$ -BN [blue lines in Figs. 3(a)]. The band dispersion was computed within the  $GW$  approximation [56] of the *ab initio* many-body perturbation theory [57], in which the self-energy is given by the product of the one-particle Green's function  $G$  and the dynamically screened Coulomb interaction  $W$ . While the Kohn-Sham eigenvalues of density-functional theory cannot be rigorously interpreted as the removal energies measured in ARPES, from the poles of the Green's function  $G$ , one obtains the quasiparticle energies that form the measured band structure [58]. The comparison between ARPES and  $GW$  calculations in the whole three-dimensional Brillouin zone [Fig. S4(a) and S4(b)] allowed us to determine the value  $0.3\pi/c$  of the  $k_z$  wave-vector component perpendicular to the  $\bar{\Gamma}KM$  plane that

was measured in the experiment. From the excellent agreement between the measured band structure and the  $GW$  calculations [Figs. 3(a) and S3(c)], we conclude that the epitaxial graphene is an ideal substrate to study bulk  $h$ -BN band structure.

A further insight into the band structure is provided by the intensity maps at constant energy [59]. Figure 4 shows the experimental data collected here compared to the theoretical results for three different binding energy values, where the color code represents the intensity. Thanks to images from 2.4 to 4.35 eV, we can observe different parallel cuts of the band structure around  $\bar{K}$  ( $\bar{K}'$ ) points, characteristic of multilayer bulk  $h$ -BN. At Fermi energy  $E_F$ , the intensity map shows no signature near the  $\bar{K}$  points of the first Brillouin zone, thus highlighting that the Fermi level lies deep inside the gap of the  $h$ -BN flakes. When the binding energy was increased to 2.5 eV, the map shows the presence of six points [Fig. 4(a)]. The absence of a graphene substrate ( $1\times 1$ ) signature is due to the thick  $h$ -BN multilayer, which completely attenuates the photoelectrons from the underlayer. When the binding energy was increased to 4 eV [Fig. 4(b)], these objects expanded and acquired a triangular warping shape. As the energy changed to 4.35 eV, the constant energy map deviated to a circular shape centered on the  $\bar{\Gamma}$  point of the BZ.

Finally, the experimental and theoretical data confirmed the splitting of the  $\pi$  states along the  $\bar{\Gamma}\bar{K}$  and  $\bar{K}\bar{M}$  directions. These two parabolic bands dispersed along  $\bar{\Gamma}\bar{K}$  and  $\bar{K}\bar{M}$ , thus revealing the major difference with a  $h$ -BN monolayer, where only one  $\pi$  band is present along these directions with a maximum near the  $\bar{K}$  ( $\bar{K}'$ ) point, 2.9 eV below the Fermi level. Considering the 2.5-eV energy difference between the Fermi level and the top of the valence band and the 6-eV quasiparticle band gap, we can infer that our sample had a residual

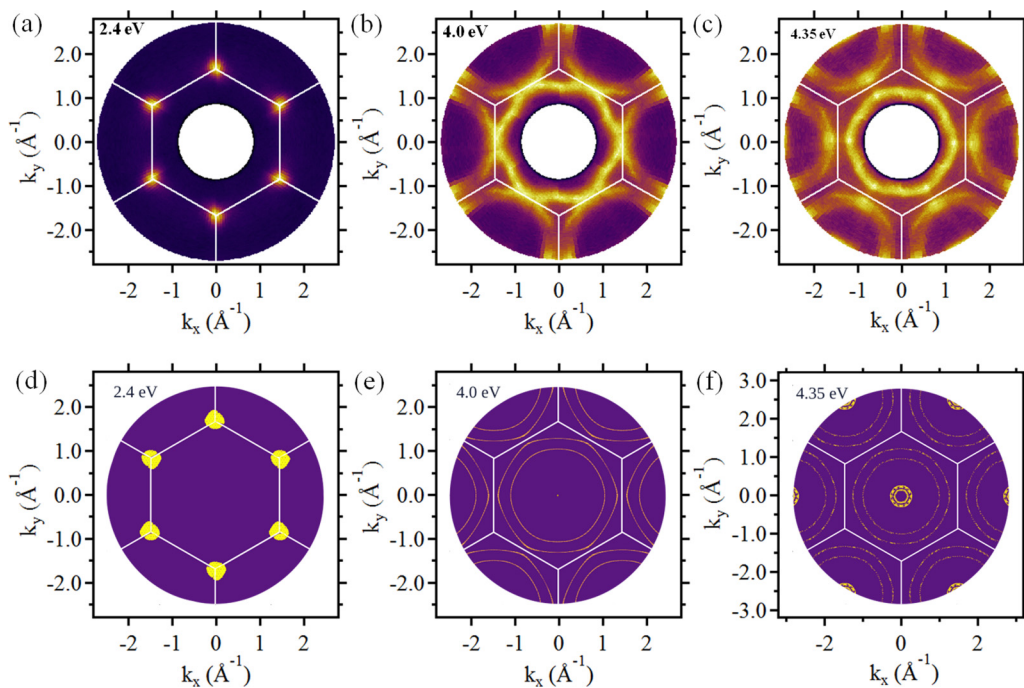


FIG. 4. 2D structure of the bulk  $h$ -BN band, as measured on the sample: (a)–(c) Local 2D  $k_{//}$  projection of the first Brillouin zone at binding energies of 2.4, 4, and 4.35 eV, respectively, obtained by measuring one-fourth of the BZ and mirroring two times to obtain the full BZ. (d)–(f) Theoretical calculations of (a)–(c) projections, at the same binding energies.

*p*-type doping character typical of bulk *h*-BN. Moreover, a good agreement between theory and experiment has been found for the electron effective mass in the  $\Gamma \rightarrow K$  direction near the *K* point; this mass is equal to about  $-0.49m_e$  (where  $m_e$  is the electron mass).

The determination of the band structure and the top of the valence band of *h*-BN represents real advances in the design of heterostructures based on *h*-BN and 2D material layers. The performance of these heterostructures is governed by the band alignment and the interlayer interaction between the different materials. However, before using these alternative materials in actual applications, the physics of such structures must be understood, particularly a deep understanding of the electronic structure of these heterojunctions, since one of the key parameters in designing the heterojunction relies on the determination of band offset. Indeed, the very low dimensionality of these systems (a few angstroms thick) prohibits the formation of a depletion region. The absence of a depletion region leads to a different operational mode of the junction that has not yet been studied on the atomic scale.

#### IV. CONCLUSIONS

In summary, we have successfully conducted high-resolution nano-ARPES on *h*-BN. Thanks to the graphene underlayer, the absence of an electrostatic charging effect of the transferred *h*-BN flakes, as well as its high structural

and electronic qualities, has made it possible to study the electronic structure in the low-energy range. The electronic properties of *h*-BN were characterized using XPS/ARPES and micro-Raman spectroscopy, showing that the quality of the *h*-BN flakes on graphene is very similar to single-crystalline *h*-BN. The electronic band structure shows a valence-band maximum near the  $\bar{K}$  ( $\bar{K}'$ ) point; revealing these values is crucial in the design of all possible heterojunctions. The study of *h*-BN band structure shows that epitaxial graphene is an ideal substrate to study bulk *h*-BN band structure. Thus, the deposition of *h*-BN flakes on graphene films provides the possibility of obtaining their wave-vector-resolved electronic structure, as reported here, as well as a way to study their physical properties in a devicelike context. These results would be extremely valuable in designing, fabricating, and optimizing these materials for future device applications.

#### ACKNOWLEDGMENTS

This work was supported by H2DH grants and by a Marie Curie FP7 Integration Grant within the 7th European Union Framework Programme. We also acknowledge support from GANEX (Grant No. ANR-11-LABX-0014) and labex NanoSaclay (Grant No. ANR-10-LABX-0035). G.F. acknowledges the grant *Chaire Énergies Durables* from École Polytechnique. Computation time was granted by GENCI (Project No. 0544).

- 
- [1] L. Britnell, R. V Gorbachev, R. Jalil, B. D. Belle, F. Schedin, M. I. Katsnelson, L. Eaves, S. V Morozov, A. S. Mayorov, N. M. R. Peres, A. H. C. Neto, J. Leist, A. K. Geim, L. A. Ponomarenko, and K. S. Novoselov, *Nano Lett.* **12**, 1707 (2012).
- [2] C. R. Dean, A. F. Young, I. Meric, C. Lee, L. Wang, S. Sorgenfrei, K. Watanabe, T. Taniguchi, P. Kim, K. L. Shepard, and J. Hone, *Nat. Nanotechnol.* **5**, 722 (2010).
- [3] A. S. Mayorov, R. V Gorbachev, S. V. Morozov, L. Britnell, R. Jalil, L. A. Ponomarenko, P. Blake, K. S. Novoselov, K. Watanabe, T. Taniguchi, and A. K. Geim, *Nano Lett.* **11**, 2396 (2011).
- [4] Z. Liu, L. Song, S. Zhao, J. Huang, L. Ma, J. Zhang, J. Lou, and P. M. Ajayan, *Nano Lett.* **11**, 2032 (2011).
- [5] L. Li, I. Lee, D. Lim, M. Kang, G.-H. Kim, N. Aoki, Y. Ochiai, K. Watanabe, and T. Taniguchi, *Nanotechnology* **26**, 295702 (2015).
- [6] S. Wang, X. Wang, and J. H. Warner, *ACS Nano* **9**, 5246 (2015).
- [7] Y.-C. Lin, N. Lu, N. Perea-Lopez, J. Li, Z. Lin, X. Peng, C. H. Lee, C. Sun, L. Calderin, P. N. Browning, M. S. Bresnehan, M. J. Kim, T. S. Mayer, M. Terrones, and J. A. Robinson, *ACS Nano* **8**, 3715 (2014).
- [8] M. Okada, T. Sawazaki, K. Watanabe, T. Taniguchi, and H. Hibino, *ACS Nano* **8**, 8273 (2014).
- [9] A. Pakdel, Y. Bando, and D. Golberg, *Chem. Soc. Rev.* **43**, 934 (2014).
- [10] S. J. Haigh, A. Gholinia, R. Jalil, S. Romani, L. Britnell, D. C. Elias, K. S. Novoselov, L. A. Ponomarenko, A. K. Geim, and R. Gorbachev, *Nat. Mater.* **11**, 764 (2012).
- [11] K. Watanabe, T. Taniguchi, and H. Kanda, *Nat. Mater.* **3**, 404 (2004).
- [12] S. Yuan, C. Journet, S. Linas, V. Garnier, P. Steyer, S. Benayoun, A. Brioude, and B. Toury, *Crystals* **6**, 55 (2016).
- [13] X. Li, S. Sundaram, Y. El Gmili, T. Ayari, R. Puybaret, G. Patriarche, P. L. Voss, J. P. Salvestrini, and A. Ougazzaden, *Cryst. Growth Des.* **16**, 3409 (2016).
- [14] A. Nagashima, N. Tejima, Y. Gamou, T. Kawai, and C. Oshima, *Phys. Rev. B* **51**, 4606 (1995).
- [15] D. Usachov, V. K. Adamchuk, D. Haberer, A. Grüneis, H. Sachdev, A. B. Preobrajenski, C. Laubschat, and D. V. Vyalikh, *Phys. Rev. B* **82**, 075415 (2010).
- [16] A. Nagashima, N. Tejima, Y. Gamou, T. Kawai, and C. Oshima, *Phys. Rev. Lett.* **75**, 3918 (1995).
- [17] H. Sediri, D. Pierucci, M. Hajlaoui, H. Henck, G. Patriarche, Y. J. Dappe, S. Yuan, B. Toury, R. Belkhou, M. G. Silly, F. Sirotti, M. Boutchich, and A. Ouerghi, *Sci. Rep.* **5**, 16465 (2015).
- [18] F. Polack, M. Silly, C. Chauvet, B. Lagarde, N. Bergéard, M. Izquierdo, O. Chubar, D. Krizmancic, M. Ribbens, J.-P. Duval, C. Basset, S. Kubsky, F. Sirotti, R. Garrett, I. Gentle, K. Nugent, and S. Wilkins, *AIP Conf. Proc.* **1234**, 185 (2010).
- [19] T. D. Thomas, R. Püttner, H. Fukuzawa, G. Prümper, K. Ueda, E. Kukk, R. Sankari, J. Harries, Y. Tamenori, T. Tanaka, M. Hoshino, and H. Tanaka, *J. Chem. Phys.* **127**, 244309 (2007).
- [20] K. C. Prince, M. Vondráček, J. Karvonen, M. Coreno, R. Camilloni, L. Avaldi, and M. de Simone, *J. Electron Spectrosc. Relat. Phenom.* **101–103**, 141 (1999).

- [21] See Supplemental Material at <http://link.aps.org/supplemental/10.1103/PhysRevB.95.085410> for details on experimental setup and further photoemission results.
- [22] X. Gonze, G. M. Rignanese, M. Verstraete, J. M. Beuken, Y. Pouillon, R. Caracas, F. Jollet, M. Torrent, G. Zerah, M. Mikami, P. Ghosez, M. Veithen, J. Y. Raty, V. Olevano, F. Bruneval, L. Reining, R. Godby, G. Onida, D. R. Hamann, and D. C. Allan, *Zeitschrift für Kristallographie - Crystalline Materials* **220**, 558 (2005).
- [23] X. Blase, A. Rubio, S. G. Louie, and M. L. Cohen, *Phys. Rev. B* **51**, 6868 (1995).
- [24] G. Cappellini, G. Satta, M. Palummo, and G. Onida, *Phys. Rev. B* **64**, 035104 (2001).
- [25] B. Arnaud, S. Lebègue, P. Rabiller, and M. Alouani, *Phys. Rev. Lett.* **96**, 026402 (2006).
- [26] L. Wirtz, A. Marini, and A. Rubio, *Phys. Rev. Lett.* **96**, 126104 (2006).
- [27] C. Berger, Z. Song, X. Li, X. Wu, N. Brown, C. Naud, D. Mayou, T. Li, J. Hass, A. N. Marchenkov, E. H. Conrad, P. N. First, and W.A. de Heer, *Science* **312**, 1191 (2006).
- [28] M. Sprinkle, M. Ruan, Y. Hu, J. Hankinson, M. Rubio-Roy, B. Zhang, X. Wu, C. Berger, and W. A. de Heer, *Nat. Nanotechnol.* **5**, 727 (2010).
- [29] C. Virojanadara, M. Syväjärvi, R. Yakimova, L. I. Johansson, A. A. Zakharov, and T. Balasubramanian, *Phys. Rev. B* **78**, 245403 (2008).
- [30] J. Hicks, A. Tejada, A. Taleb-Ibrahimi, M. S. Nevius, F. Wang, K. Shepperd, J. Palmer, F. Bertran, P. Le Fèvre, J. Kunc, W. A. de Heer, C. Berger, and E. H. Conrad, *Nat. Phys.* **9**, 49 (2012).
- [31] K. V Emtsev, A. Bostwick, K. Horn, J. Jobst, G. L. Kellogg, L. Ley, J. L. McChesney, T. Ohta, S. A. Reshanov, J. Röhrl, E. Rotenberg, A. K. Schmid, D. Waldmann, H. B. Weber, and T. Seyller, *Nat. Mater.* **8**, 203 (2009).
- [32] N. Camara, J.-R. Huntzinger, G. Rius, A. Tiberj, N. Mestres, F. Pérez-Murano, P. Godignon, and J. Camassel, *Phys. Rev. B* **80**, 125410 (2009).
- [33] E. Pallecchi, F. Lafont, V. Cavaliere, F. Schopfer, D. Maily, W. Poirier, and A. Ouerghi, *Sci. Rep.* **4**, 4558 (2014).
- [34] S. Lara-Avila, K. Moth-Poulsen, R. Yakimova, T. Bjørnholm, V. Fal'ko, A. Tzalenchuk, and S. Kubatkin, *Adv. Mater.* **23**, 878 (2011).
- [35] T. Ohta, A. Bostwick, T. Seyller, K. Horn, and E. Rotenberg, *Science* **313**, 951 (2006).
- [36] B. Lalmi, J. C. Girard, E. Pallecchi, M. Silly, C. David, S. Latil, F. Sirotti, and A. Ouerghi, *Sci. Rep.* **4**, 4066 (2014).
- [37] E. Pallecchi, M. Ridene, D. Kazazis, F. Lafont, F. Schopfer, W. Poirier, M. O. Goerbig, D. Maily, and A. Ouerghi, *Sci. Rep.* **3**, 1791 (2013).
- [38] H. Henck, D. Pierucci, Z. Ben Aziza, M. G. Silly, B. Gil, F. Sirotti, G. Cassabois, and A. Ouerghi, *Appl. Phys. Lett.* **110**, 023101 (2017).
- [39] N. L. McDougall, R. J. Nicholls, J. G. Partridge, and D. G. McCulloch, *Microsc. Microanal.* **20**, 1053 (2014).
- [40] R. W. Lynch and H. G. Drickamer, *J. Chem. Phys.* **44**, 181 (1966).
- [41] J. Koskelo, G. Fugallo, M. Hakala, M. Gatti, F. Sottile, and P. Cudazzo, *Phys. Rev. B* **95**, 035125 (2017).
- [42] K. H. Lee, H.-J. Shin, J. Lee, I. Lee, G.-H. Kim, J.-Y. Choi, and S.-W. Kim, *Nano Lett.* **12**, 714 (2012).
- [43] Q. Wu, J.-H. Park, S. Park, S. J. Jung, H. Suh, N. Park, W. Wongwiriyanpan, S. Lee, Y. H. Lee, and Y. J. Song, *Sci. Rep.* **5**, 16159 (2015).
- [44] M. C. Polo, E. Martinez, J. Esteve, and J. L. Andfjar, *Diamond Relat. Mater.* **7**, 376 (1997).
- [45] K. S. Park, D. Y. Lee, K. J. Kim, and D. W. Moon, *Appl. Phys. Lett.* **70**, 315 (1997).
- [46] W. Lei, D. Portehault, R. Dimova, and M. Antonietti, *J. Am. Chem. Soc.* **133**, 7121 (2011).
- [47] R. Sevak Singh, R. Yingjie Tay, W. Leong Chow, S. Hon Tsang, G. Mallick, and E. H. Tong Teo, *Appl. Phys. Lett.* **104**, 163101 (2014).
- [48] T. Sugino and T. Tai, *Jpn. J. Appl. Phys.* **39**, L1101 (2000).
- [49] T. Sugino, T. Tai, and Y. Etou, *Diamond Relat. Mater.* **10**, 1375 (2001).
- [50] I. Caretti and I. Jiménez, *J. Appl. Phys.* **110**, 023511 (2011).
- [51] W. J. Pan, J. Sun, H. Ling, N. Xu, Z. F. Ying, and J. D. Wu, *Appl. Surf. Sci.* **218**, 298 (2003).
- [52] W. Orellana and H. Chacham, *Phys. Rev. B* **63**, 125205 (2001).
- [53] J. Avila, M. C. Asensio, and C. Taylor, *Synchrotron Radiat. News* **27**, 24 (2014).
- [54] J. Avila, I. Razado-Colambo, S. Lorcy, B. Lagarde, J.-L. Giorgetta, F. Polack, and M. C. Asensio, *J. Phys. Conf. Ser.* **425**, 192023 (2013).
- [55] E. Doni and G. P. Parravicini, *Nuovo Cim. B* **64**, 117 (1969).
- [56] L. Hedin, *Phys. Rev.* **139**, A796 (1965).
- [57] R. M. Martin, L. Reining, and D. M. Ceperley, *Interacting Electrons: Theory and Computational Approaches* (Cambridge University Press, Cambridge, 2016).
- [58] G. Fugallo, M. Aramini, J. Koskelo, K. Watanabe, T. Taniguchi, M. Hakala, S. Huotari, M. Gatti, and F. Sottile, *Phys. Rev. B* **92**, 165122 (2015).
- [59] D. Pierucci, H. Henck, J. Avila, A. Balan, C. H. Naylor, G. Patriarche, Y. J. Dappe, M. G. Silly, F. Sirotti, A. T. Charlie Johnson, M. C. Asensio, and A. Ouerghi, *Nano Lett.* **16**, 4054 (2016).